A laboratory study of the effect of Fe(II)-bearing minerals on nuclear magnetic resonance (NMR) relaxation measurements

Kristina Keating[1] and Rosemary Knight[2]

ABSTRACT

A laboratory study was conducted to measure the effect of the mineralogic form and concentration of iron(II) [Fe(II)] minerals on nuclear magnetic resonance (NMR) relaxation rates of water-saturated sand mixtures. We measured mixtures of quartz sand and three common Fe(II)-bearing minerals in granular form: siderite ($FeCO_3$), pyrite (FeS_2), and pyrrhotite ($Fe_{1-x}S$; $0 < x < 0.2$) at two concentrations of iron by weight. The NMR response of these samples was used to calculate four transverse relaxation rates for each Fe(II) mineral mixture: total mean log, bulk fluid, diffusion, and surface relaxation rates. The surface area of the samples was used to calculate the surface relaxivity of the sample and the magnetically active surface. For each iron mineral, the mean log and surface relaxation rates were greater for samples with higher Fe(II) concentration. For the siderite, pyrrhotite, and high-concentration pyrite mixtures, surface relaxation was the dominant relaxation mechanism. Bulk fluid relaxation contributed significantly to the total relaxation for the siderite and pyrite mixtures; for the low-concentration pyrite mixtures, bulk fluid relaxation was the dominant relaxation mechanism. For the pyrrhotite mixtures, the diffusion relaxation rate was nonzero and slower than the surface relaxation rate; for the siderite and pyrite mixtures, the diffusion relaxation rate was zero. Surface relaxivity calculations revealed that, for the pyrite mixtures, relaxation occurred in the fast diffusion regime; for the siderite and pyrrhotite mixtures, relaxation did not occur in the fast diffusion regime. The range of surface relaxivity values calculated depends on mineralogic form. We conclude that Fe(II) concentration and mineralogic form are important factors in determining relaxation rate.

INTRODUCTION

The proton nuclear magnetic resonance (NMR) relaxation measurement is used in earth sciences to explore for and evaluate petroleum and groundwater resources. NMR borehole logging instruments have been used since the 1960s to detect water and hydrocarbons and to determine the porosity and permeability of petroleum reservoirs and, more recently, groundwater aquifers (e.g., Brown et al., 1960; Kleinberg et al., 1992; Clayton, 2006). Another field method, magnetic resonance sounding (MRS), is used to estimate the water content and permeability in the top 100 m of the subsurface using a wire loop laid out on the earth's surface (Schirov et al., 1991; Legchenko et al., 2004). NMR laboratory studies improve our interpretation of NMR logging and MRS data, and they have been used to explore new applications. Most recently, laboratory studies have demonstrated the use of NMR relaxation measurements to monitor microbially induced changes in chemistry and pore volume of soils (Jaeger et al., 2006) and abiotic geochemical reactions (Keating et al., 2008)

The NMR relaxation experiment for a water-saturated porous material consists of observing the response of hydrogen nuclei (protons) in the pore water to a perturbation by an external magnetic force and measuring the precessional motion of the protons during their return or relaxation to equilibrium. The rate of this relaxation is related to the surface-area-to-volume ratio of the pore space S/V; this relationship has been used to link NMR relaxation rate to permeability (e.g., Timur, 1969). Two factors that can affect the relationship between NMR relaxation rate and S/V are the presence of paramagnetic species (i.e., atoms with unpaired electrons) and the presence of magnetic minerals with high values of magnetic susceptibility. Iron-bearing minerals can contain paramagnetic species [e.g., Fe(III)] and can have high values of magnetic susceptibility (e.g.,

magnetite), so there is a clear need to understand how iron minerals affect the NMR measurement. This is the focus of our research.

Iron is widespread in subsurface geologic materials, with concentrations in sediments and sedimentary rocks ranging from less than 0.1% to greater than 10% (Cornell and Schwertman, 2003). In the subsurface, iron primarily exists in two oxidation states: Fe(III) and Fe(II). Iron in these oxidation states can be present in the aqueous phase — sorbed to the solid surface of mineral grains and as part of the crystal structure of minerals. Fe(III) is mainly found in oxidizing environments; Fe(II) is mainly found in reducing environments. There are also a few mixed-valence minerals that contain both Fe(II) and Fe(III) (e.g., magnetite, pyrrhotite).

The effect of aqueous Fe(III), or $Fe^{3+}(aq)$, on the NMR response of a pore fluid is well established: The relaxation rate of water increases linearly with the concentration of the paramagnetic species $Fe^{3+}(aq)$ (Bloembergen et al., 1948; Bryar and Knight, 2002). In natural systems, however, the concentration of Fe(III) in the pore water is generally too small to influence an NMR measurement. This is because of the low solubility of most Fe(III)-bearing minerals and the pH of natural water (Vogeley and Moses, 1992). The presence of aqueous Fe(II), or $Fe^{2+}(aq)$, which is not a paramagnetic species, does not affect the relaxation rate of water (Bryar and Knight, 2002).

When Fe(III) is present on the surface of the solid phase, the NMR relaxation rate of water in a porous geologic material depends on the concentration and mineralogic form of Fe(III). Foley et al. (1996) and Bryar et al. (2000) show that, for any given iron mineral, the relaxation rate is proportional to the concentration of Fe(III) on the surface of the solid phase. Work by Keating and Knight (2007) clearly shows that, in addition to this established dependence on Fe(III) concentration, the mineral form of Fe(III) also affects the NMR relaxation rate of pore water. Understanding the effect of Fe(III) on NMR signals is also of interest in the medical community; many studies have been conducted to understand how the presence of iron affects the NMR relaxation rate of protons in biological tissue (e.g., Gossuin et al., 2004). Publications from the medical community are consistent with the geophysical community; they show that the NMR relaxation rate increases with Fe(III) concentration (e.g., Gossuin et al., 2004) and depends on the mineralogic form of iron (e.g., Yilmaz et al., 1990; Babes et al., 1999; Gossuin et al., 2002).

Although these studies investigate the effect of the concentration of Fe(III) and the mineralogic form of Fe(III) on NMR relaxation rates, no published studies address the effect of Fe(II)-bearing minerals on the NMR relaxation rate of pore water. Although the addition of $Fe^{2+}(aq)$ has not been shown to enhance the relaxation rate of water, results from one study indicate that the presence of the Fe(II)-bearing mineral pyrite can enhance relaxation (Bryar and Knight, 2002). Our study was designed to address this gap in the literature and to explore the effect of the concentration and mineralogic form of Fe(II)-bearing minerals on the NMR relaxation rate of water in a porous material.

We selected for our measurements a set of naturally abundant Fe(II)-bearing minerals. Two of the minerals studied, siderite ($FeCO_3$) and pyrite (FeS_2), are pure Fe(II)-bearing minerals. The third mineral, pyrrhotite ($Fe_{1-x}S$; $0 < x < 0.2$), is a mixed-valence mineral primarily containing Fe(II) (Pratt et al., 1994). Each of the minerals was mixed with pure quartz sand at two concentrations to assess the relationship between Fe(II) concentration and NMR relaxation rate. Understanding the effect of these minerals on the NMR relaxation rate will improve our ability to interpret NMR measurements on geologic materials in the laboratory and in the field.

NMR RELAXATION THEORY

The NMR relaxation phenomenon results from the fact that all nuclei with an odd number of protons or neutrons possess a nuclear spin angular momentum. The hydrogen nucleus, with a single proton, is of particular interest because of its presence in water. In a static magnetic field, the nuclear spins of a fraction of the protons in water will align with the static field, resulting in a total magnetization that is proportional to the number of protons in the sample. The NMR experiment involves applying an oscillating magnetic field, tuned to detect hydrogen, to the sample for a short time. During the experiment, the nuclear spins diverge from, and then relax back to, their equilibrium position. This results in a measurable change in the bulk nuclear magnetization over time t. In our study, we focused on the spin-spin or transverse relaxation, the parameter measured by most well-logging and surface-based NMR instruments.

For water in a single pore, the magnetization exhibits a multiple exponential decay (Brownstein and Tarr, 1979):

$$M(t) = \sum_{j=0}^{n} M_j e^{-tT_{2j}^{-1}}, \qquad (1)$$

where M_j is the magnetization of the jth mode and T_{2j}^{-1} is the relaxation rate of the jth mode. Equation 1 is ordered such that $T_{20}^{-1} < T_{21}^{-1} < T_{22}^{-1}\ldots$. The initial magnetization, $M(0) = \Sigma M_j$, is proportional to the total water content in the pore.

Brownstein and Tarr (1979) define three relaxation regimes for the exponential decay. In the first regime, the fast diffusion regime, the protons can move to and interact with the surface of the pore within the time scale of the experiment. The relaxation behavior in the fast diffusion regime, in the absence of magnetic-field inhomogeneities, depends primarily on the S/V and the surface relaxivity, or the ability of a surface to enhance relaxation. In this regime, the relaxation behavior is described by a single mode, and $M(t)$ is a monoexponential function. For the second regime, the slow diffusion regime, the relaxation behavior, in the absence of magnetic field inhomogeneities, depends primarily on the diffusion coefficient D. In this regime, most of the magnetization is in the first mode (i.e., most of the protons relax with a rate of T_{20}^{-1}), but 10–40% percent of the magnetization is in the higher modes. In the third regime, the intermediate diffusion regime, most of the magnetization is again in the first mode, but a few percent of the total magnetization is in higher modes.

For water in a porous geologic material, the measured signal intensity $I(t)$ is a multiexponential decay (Timur, 1969):

$$I(t) = \sum I_{0i} e^{-tT_{2i}^{-1}}, \qquad (2)$$

where I_{0i} is proportional to the number of protons relaxing with a relaxation rate of T_{2i}^{-1}. The inverse of the relaxation rate is the relaxation time T_{2i}.

In equation 2, the initial signal intensity $I(0) = \Sigma I_{0i}$, is proportional to the water content detected by the NMR relaxation measurement. The NMR-detected water content can be less than the true water content in the measured sample when the applied pulse is imperfectly tuned or when some of the protons relax so quickly that the signal from these protons is lost in the instrument dead time (the time until the first datum is acquired) (Kleinberg, 2001).

In the case of fast diffusion, each pore type is represented by a single exponential in equation 2, and the relaxation-time distribution (the plot of I_{0i} versus T_{2i}) represents the distribution of pore environ-

ments in the geologic material (Kleinberg et al., 1994; Arns, 2004). In practice, it is often assumed that the chemical environment does not vary from pore to pore, and the relaxation-time distribution is taken to represent the pore-size distribution of the material (e.g., Arns, 2004).

The NMR relaxation behavior of a sample is typically represented by one value, calculated from the distribution of relaxation times as the weighted arithmetic mean of log T_2, or T_{2ML}[log T_{2ML} = $\Sigma(I_{0i} \log T_{2i})/\Sigma I_{0i}$]. T_{2ML}^{-1} is described as a sum of three relaxation rates (Brownstein and Tarr, 1979; Kleinberg and Horsfield, 1990):

$$T_{2ML}^{-1} = T_{2B}^{-1} + T_{2S}^{-1} + T_{2D}^{-1}, \qquad (3)$$

where T_{2B}^{-1} is the bulk fluid relaxation rate, T_{2D}^{-1} is the diffusion relaxation rate, and T_{2S}^{-1} is the surface relaxation rate.

The bulk fluid relaxation rate of water is caused by dipole-dipole molecular interactions. For a fluid, the magnitude of T_{2B}^{-1} depends on temperature, pH, and viscosity (via the reduction of mobility), and the concentration of dissolved paramagnetic species (e.g., dissolved oxygen, Mn^{2+} ions, and Fe^{3+} ions) (Bloembergen et al., 1948; Bryar and Knight, 2002; Dunn et al., 2002). Although the magnitude of T_{2B}^{-1} is affected by the properties of the pore fluid, the magnitudes of T_{2D}^{-1} and T_{2S}^{-1} are affected by the properties of the solid phase. In the next sections, we briefly review the way in which the properties of geologic materials affect diffusion and surface relaxation rates.

Diffusion relaxation

Diffusion relaxation arises when the relaxing protons diffuse through a nonuniform magnetic field; the nonuniform magnetic field causes the protons to dephase, thus enhancing relaxation. The diffusion relaxation rate T_{2D}^{-1} is described by (Carr and Purcell, 1954; Kleinberg and Horsfield, 1990)

$$T_{2D}^{-1} = \frac{D}{12}(\gamma G t_E)^2, \qquad (4)$$

where G is the average internal gradient of the nonuniform magnetic field, D is the diffusion coefficient of water, γ is the gyromagnetic ratio, and t_E is the echo time. Equation 4 is valid in the unrestricted free diffusion regime (i.e., when the average distance traveled by a proton during the echo time is much smaller than both the average distance traveled before dephasing by 1 radian and the average pore size) as described by Anand and Hirasaki (2008). G arises because of inhomogeneities in the static magnetic field and because of differences between the magnetic susceptibility χ_v of the water, which contains the diffusing protons, and the surrounding solid geologic material.

The diffusion relaxation mechanism does not contribute to the total relaxation response for all minerals. However, in the presence of magnetic minerals with large susceptibility values (e.g., magnetite), diffusion relaxation is significant and results in a detectable T_{2D}^{-1} (Keating and Knight, 2007, 2008). The echo time is a timing parameter in the Carr-Purcell-Meiboom-Gill (CPMG) pulse sequence (Carr and Purcell, 1954; Meiboom and Gill, 1958).

More advanced data acquisition methods have been developed to characterize internal magnetic fields in pores and to understand pore geometry in the presence of magnetic field gradients (e.g., Hurlimann et al., 2002; Song, 2003); however, equation 4 is still commonly used to understand the effect of internal magnetic field gradients

on T_{2ML}^{-1} (e.g., Zhang et al., 2003; Stingaciu et al., 2009). We note that the magnetic field gradients induced by minerals with large susceptibility values will decrease with magnetic field strength, implying that T_{2D}^{-1} values determined from measurements made using a 2-MHz NMR analyzer may be very different from T_{2D}^{-1} values determined from measurements made at other magnetic field strengths. To our knowledge, no completed studies confirm this result.

Published information about the magnetic properties of the materials used in this study is given in Table 1. Water and quartz are diamagnetic (i.e., do not have unpaired electrons). Of the Fe(II)-bearing minerals used in this study, siderite and pyrite are paramagnetic (i.e., have unpaired electrons whose spins are randomly oriented and whose magnetization increases linearly with magnetic field strength) (Klein, 2002). Pyrrhotite is ferrimagnetic (i.e., has unpaired electrons whose spins are aligned parallel or antiparallel in such a way as to result in a nonzero net magnetization); however, when the number of iron atoms is equal to the number of sulfur atoms in pyrrhotite, the mineral (troilite) becomes antiferromagnetic (i.e., has unpaired electrons whose spins are aligned parallel or antiparallel such that the net magnetization is zero) (Klein, 2002). The magnetic susceptibility for common iron-bearing minerals can be as low as 35×10^{-6} SI for pyrite to as high as 5.7 SI for magnetite (Hunt et al., 1995; Lide, 2007). The magnetic susceptibilities for quartz and water are less than zero. For the iron minerals used in our study, pyrite can have the lowest magnetic susceptibility and pyrrhotite can have the highest (Hunt et al., 1995).

Surface relaxation

The surface relaxation rate is determined by the spin-spin interaction between water protons within a pore space and paramagnetic sites on the solid surface. For the water-saturated Fe(III) minerals we studied earlier (Keating and Knight, 2007, 2008), surface relaxation is the dominant relaxation mechanism, where "dominant" means having the fastest relaxation rate.

The equation describing T_{2S}^{-1} depends on the diffusion regime in which relaxation occurs. In the fast diffusion regime, T_{2S}^{-1} is a function of the S/V; this relationship allows NMR data to be used to estimate permeability in geophysical applications (Timur, 1969). The surface relaxation rate is given by (Senturia and Robinson, 1970; Brownstein and Tarr, 1979)

$$T_{2S}^{-1} = \rho_2 \frac{S}{V}, \qquad (5)$$

where ρ_2 is the surface relaxivity of a sample, which is a measure of the extent to which the solid surface of the pore space enhances the

Table 1. Magnetic properties and range of magnetic susceptibility χ_v values for the minerals used in this study.

Material	Magnetic property[a]	χ_v[a] ($\times 10^{-6}$ SI)
Quartz (SiO_2)	Diamagnetic	-17 to -13
Siderite ($FeCO_3$)	Paramagnetic	1300 to 11,000
Pyrite (FeS_2)	Paramagnetic	35 to 5000
Pyrrhotite ($Fe_{1-x}S$; $0 < x < 0.2$)	Ferrimagnetic	460 to 1.4×10^6
Troilite (FeS)	Antiferromagnetic	610 to 1700

[a]From Hunt et al. (1995)

relaxation of the pore water. Expression 5 implies that the surface of the pore space can be described by a single ρ_2 value, suggesting a relatively homogeneous distribution of paramagnetic sites on the surface. But in many geologic materials, it is reasonable to assume that the surface of the pore space will be highly heterogeneous, with variation in ρ_2 from changes in mineralogy.

In our study, we consider specifically the case of a mixture of two types of mineral grains with different ρ_2 values. We refer to the grains with relatively high ρ_2 values as magnetically active and the grains with relatively low ρ_2 values as magnetically inactive. Surface relaxation primarily occurs through diffusion of the protons to the surfaces of the magnetically active grains, so the surface relaxation rate becomes

$$\frac{1}{T_{2S}} = \rho_{2M} \frac{S_M}{V}, \tag{6}$$

where ρ_{2M} is the surface relaxivity of the magnetically active grains and S_M/V is the ratio of the surface area of the magnetically active grains to the total pore volume (Foley et al., 1996). We calculate and compare ρ_2 and ρ_{2M}.

For relaxation to occur in the fast diffusion regime, the relationship $\rho_2 a/D \ll 1$ must hold, where a is a measure of the distance a proton needs to travel to reach a paramagnetic site. Here, we consider two ways of representing ρ_2. We first treat the pore surface as homogeneous and describe it using a single ρ_2 value (from equation 5). We then treat the pore surface as a mix of magnetically active and inactive grains, and we calculate ρ_{2M} using equation 6.

In the slow diffusion regime, where $\rho_2 a/D \gg 10$, the surface relaxation rate is a function of the diffusion coefficient and is no longer represented by a single value. Brownstein and Tarr (1979) show that the zero-mode relaxation rate $T_{2S0}{}^{-1}$ (i.e., the slowest relaxation rate) is given by (Brownstein and Tarr, 1979)

$$\frac{1}{T_{2S0}} = \frac{1}{\alpha} \frac{D}{\alpha^2}, \tag{7}$$

where α is a function of the geometry of the pore space ($\alpha \sim 1/3$ for spherical pores). In the slow-diffusion regime, the initial relaxation rate (i.e., the highest mode or shortest relaxation rate) is given by $T_{2i}{}^{-1} = \rho_2 S/V$. Because $T_{2ML}{}^{-1}$ is less than $T_{2i}{}^{-1}$, this implies that, in

the slow diffusion regime, equation 5 provides a lower bound for the surface relaxivity.

In the intermediate regime, where $1 \ll \rho_2 a/D \ll 10$, the contribution to the signal intensity from the modes for $n \geq 1$ is on the order of 1% (Brownstein and Tarr, 1979).

The surface relaxivity is a measure of the ability of the pore surface to enhance relaxation; it can span more than three orders of magnitude. Surface relaxivity values for pure quartz sand and for samples containing Fe(III)-bearing minerals measured in previous studies are summarized in Tables 2 and 3. The clean quartz sand measured in our earlier study (Keating and Knight, 2007), which was selected because of lack of paramagnetic content, has a ρ_2 of 0.31 μm/s (Table 2).

Surface relaxivity has been described theoretically as a function of the size of the particles containing the paramagnetic species, the distance of closest approach from a paramagnetic species to a diffusing proton, and, importantly, the electron spin number of the paramagnetic species (Abragam, 1961; Gillis and Koenig, 1987). The spin number of iron depends primarily on its oxidation state; aqueous Fe(III) has a spin number of 5/2, whereas aqueous Fe(II) has a spin number of two. The electron spin number of iron also depends on the spin arrangement of the electrons in the iron atom. Siderite and pyrrhotite have Fe(II) in a high-spin arrangement (i.e., electrons in the d-orbital are unpaired) and a spin number of two. Pyrite has Fe(II) in a low-spin arrangement (i.e., all electrons in the d-orbital are paired); thus, the total electron spin number for Fe(II) in pyrite is less than two (Coey, 1988). This variation in spin number is anticipated to affect the surface relaxivity of the measured Fe(II)-bearing minerals.

It is common for natural minerals to contain impurities. Given that these impurities have a spin number different from that of iron, it is reasonable to assume the surface relaxivity of natural minerals will vary because of the presence of impurities. In siderite, manganese and magnesium can substitute for iron; in pyrite, small amounts of nickel and cobalt are common substitutes for iron (Klein, 2002). Therefore, we expect to see some effect on the ρ_2 and ρ_{2M} values of the natural Fe(II)-bearing minerals measured in this study as a result of the impurities.

Table 2. Surface relaxivity of quartz sand and Fe(III)-bearing minerals.

Solid phase	Iron concentration (wt. %)	ρ_2 (μm/s)
Quartz sand[a]	0	0.31
Goethite-coated quartz sand[a]	1	1.61
Ferrihydrite-coated quartz sand[a]	1	2.2
Lepidocrocite-coated quartz sand[a]	1	5.4
Hematite-coated quartz sand[a]	1	≥ 17.9[c]
Calcium silicates doped with hematite[b]	1	26.7

[a]From Keating and Knight (2007).
[b]Calculated from Foley et al. (1996).
[c]Relaxation for this sample did not occur in the fast diffusion regime and ρ_2 represents a lower bound on the true value; $\rho_2 a/D$ was calculated using $a = 146.4$ μm.

Table 3. Surface relaxivity of mixtures of quartz sand and magnetite.

Solid phase	Grain size (μm)	Iron concentration (wt. %)	ρ_2 (μm/s)
Magnetite and quartz sand mixture[a]	110–360	0.64	4.1
Magnetite and quartz sand mixture[a]	110–360	1.3	6.5
Magnetite and quartz sand mixture[a]	< 45	0.64	≥ 180[c]
Magnetite and quartz sand mixture[a]	< 45	1.3	≥ 250[c]
Magnetite-coated quartz sand[b]	< 0.5	0.65	≥ 292[c]

[a]From Keating and Knight (2008);
[b]From Keating and Knight (2007).
[c]Relaxation for these samples did not occur in the fast diffusion regime; ρ_{2g} represents a lower bound on the true value, and $\rho_2 a/D$ was calculated using $a = 146.4$ μm.

To understand the effect of the mineralogical form of Fe(II) on the NMR response of water, we compared T_{2ML}^{-1}, T_{2B}^{-1}, T_{2S}^{-1}, and T_{2D}^{-1} of water-saturated samples containing pure quartz and two concentrations of three different Fe(II)-bearing minerals. We also compared the relaxation-time distribution, the total initial signal intensity, ρ_2, and ρ_{2M} for each of these samples. Our laboratory results are a first step toward improving the interpretation of geophysical NMR relaxation measurements made on materials containing Fe(II)-bearing minerals.

METHODS AND MATERIALS

Materials and preparation of sample mixtures

To investigate the NMR response of sediments containing the selected Fe(II)-bearing minerals, we prepared mixtures of quartz sand combined with siderite, pyrite, and pyrrhotite. Quartz sand (99.995%, less than 40 mesh, diameter < 420 μm, silicon [IV] dioxide; supplied by Alfa Aesar) was used as an analog for a naturally occurring mineral surface. We have used this quartz sand for measurements in our laboratory, and we have fully characterized its NMR response (Bryar and Knight, 2003; Keating and Knight, 2007). The three Fe(II) minerals investigated were mixed with quartz sand at concentrations of 1% (low concentration) and 2% (high concentration) iron by weight. The initial weight percent was estimated using the pure chemical formula for each iron mineral. To account for impurities in the minerals and for dissolution of the minerals, the weight percent of iron in the siderite and pyrrhotite mixtures was also measured using the ferrozine method (described in the next section) following the NMR measurements. It was not possible to determine the weight percent of iron in pyrite by this method because the procedure requires dissolution in acid and pyrite is insoluble in acid.

The siderite and pyrite used in this study were derived from natural minerals obtained from Ward Scientific. The siderite was from a deposit in Ivigtut, Greenland; the pyrite was from a deposit in Huanzala, Peru. The density of siderite is 3.932 g/cm³, and the mass fraction of iron in siderite is 0.482 grams of iron to grams of mineral (g-iron/g-mineral); the density of pyrite is 5.010 g/cm³, and the mass fraction of iron in pyrite is 0.465 g-iron/g-mineral. Each of the minerals arrived in subcentimeter-sized pieces. The grains were reduced in size using an alumina ceramic rock grinder. The crushed minerals were sieved for 30 minutes using stainless steel sieves to isolate grains with diameters between 45 and 53 μm. The mineralogic form of the sieved siderite and pyrite was analyzed using powdered X-ray diffraction (XRD). The XRD results verified the mineralogy of the siderite and pyrite samples. Once sieved, the siderite and pyrite were moved to and stored in a sealed glove box held under anaerobic conditions to prevent oxidation of the Fe(II) to Fe(III). All further sample preparations and measurements were done under anaerobic conditions.

Iron sulfide (99.9% FeS, grain diameter < 149 μm; supplied by Fisher Scientific) was used in this study (as provided) as an analog for naturally occurring pyrrhotite. The density of pyrrhotite is 4.610 g/cm³, and the mass fraction of iron in pyrrhotite is 0.635 g-iron/g-mineral. The mineral form of the pyrrhotite was analyzed using XRD, which showed that the iron sulfide sample consisted mainly of pyrrhotite but also contained a large portion of troilite (FeS). The pyrrhotite was stored in a glove box under anaerobic conditions, and all further sample preparations and measurements were done under anaerobic conditions.

Oxygen-free, deionized water was used for the pore fluid. The oxygen was removed by boiling deionized water and subsequently purging overnight with nitrogen gas.

NMR sample preparation and measurement procedures

Three samples were prepared of each iron mineral/quartz mixture. Each sample was packed into a cylindrical Teflon sample holder (2.1-cm inner diameter and 6-cm height). Because of the difference in size between the iron-mineral grains and the quartz grains, each NMR sample contained more iron-mineral grains than quartz grains. A schematic of the samples is shown in Figure 1 (not drawn to scale).

To saturate a sample, it was submerged in a beaker of oxygen-free, deionized water (in a glove box under anaerobic conditions). The beaker was then placed in a vacuum chamber and the pressure in the chamber was reduced to 100 mm Hg for 30 minutes. The volume of water saturating the sample V_w was determined gravimetrically. After saturation, the sample was placed in a sealed glass tube (to keep the sample under anaerobic conditions) and transferred to the NMR analyzer. NMR measurements were made approximately 1 hour after saturating the samples.

NMR relaxation data were collected with a 2.2-MHz Maran Ultra NMR core analyzer (Resonance Instruments) using a CPMG pulse sequence. One data point was obtained at each echo in the CPMG pulse sequence; 20,000 echoes were used for all samples. This large number of echoes was selected to ensure that the measured signal decayed to zero. Data were collected at four echo times — 300, 400, 600, and 800 μs — with an instrument dead time of 60 μs. The data were stacked 100 times to improve the signal-to-noise ratio. The delay time between each pulse sequence was 10 s to ensure that the sample had returned to thermal equilibrium prior to the start of the pulse sequence. The total measurement time was 27, 30, 37, and 43 minutes for t_E = 300, 400, 600, and 800 μs, respectively. The measurement at an echo time of 300 μs was repeated three times; the measurements at echo times of 400, 600, and 800 μs were each repeated twice. Measurements were consistently made at 30 °C, the standard operating temperature of the instrument.

Once the NMR measurements had been completed on a saturated sample, the sample was transferred back to the sealed glove box. The pore water was removed from each sample by vacuum filtration and stored in sealed containers in the anaerobic glove box; the samples
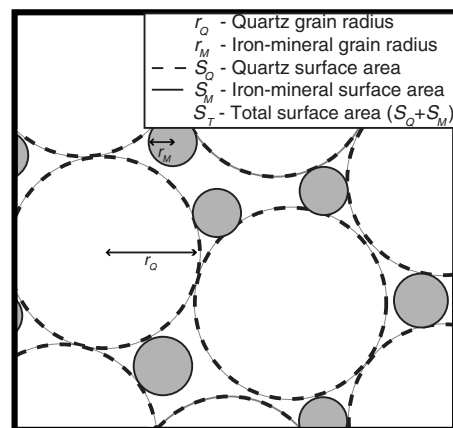

Figure 1. Schematic depicting the pore space of the measured samples. The gray spheres represent the iron-mineral grains. The white spheres represent the quartz grains. This figure is not drawn to scale.

were left to dry overnight in the glove box. The bulk-fluid relaxation rate was measured using the extracted pore water. The bulk fluid was measured at four echo times (300, 400, 600, and 800 μs); 32,000 echoes were used to ensure that the measured signal decayed to zero. All other measurement parameters were the same as for the NMR samples.

One subsample of approximately 10 g was taken from each NMR measured sample for surface-area analysis. The specific surface area S_s, defined as the surface area normalized by the mass of the sample, was measured using a Micromeritics ASAP 2020 accelerated surface area and porosimetry system; it produces reliable results for samples with a total surface area as low as 1 m². The samples used for surface-area measurements were transferred to the ASAP 2020 in a sealed glass tube to prevent oxidation. The samples were degassed with helium gas for 12 hours at 50 °C. All samples were measured using the Brunauer-Emmett-Teller (BET) adsorption method with nitrogen gas $[N_2(g)]$ as the adsorbate.

A subsample of 2 g was taken from the NMR measured mixtures of siderite and pyrrhotite; it was used to determine the Fe(II) and Fe(III) concentration within the sample. The subsample was digested in 4 mL of 6 N hydrochloric acid for one week to dissolve the iron mineral. The hydrogen chloride and iron solution was diluted (1:200) with deionized water, and the iron content of the diluted solution was measured spectrophotometrically at 562 nm by means of the ferrozine method (Stookey, 1970).

DATA ANALYSIS AND RESULTS

Physical sample properties

The measured and calculated values describing the physical sample properties for the low- and high-concentration iron mineral mixtures are shown in Table 4. The measured values are the averages of the values for each iron mineral mixture, and errors are the standard deviation. The errors for the calculated values were derived from error propagation. Also shown are the values describing the physical sample properties for the quartz sand, as published in Keating and Knight (2007).

The porosity ϕ of each sample was determined by dividing the gravimetrically determined volume of water in the sample by the volume of the sample holder. The porosity for all samples ranged from 0.48 to 0.51 and did not show any trend with iron concentration or mineralogic form.

The specific surface areas S_s of the mineral mixtures used in this study are low, ranging from 0.14 to 0.38 m²/g. For the quartz used, S_s is 0.15 m²/g (Table 4) (Keating and Knight, 2007). For each iron mineral, S_s is greater when the sample contains more iron. For the samples with a low concentration of iron, S_s ranges from 0.14 m²/g for the pyrrhotite mixture to 0.33 m²/g for the siderite mixtures. The S_s for the samples with high-concentration iron ranges from 0.21 m²/g for the pyrite mixture to 0.38 m²/g for the siderite mixture.

The S/V was determined by

$$\frac{S}{V} = \frac{S_s m_s}{V_w},$$ (8)

where m_s is the mass of the sample and V_w is the volume of water in the sample. Here, V_w was used to represent the pore space volume V; but in samples that are not fully saturated, $V_w < V$. The values of S/V are given in Table 4. Overall, the range of S/V for all iron mineral mixtures is small. For each iron mineral, S/V is greater in the mixtures with higher iron concentration. The S/V of the samples with low-concentration iron range from 0.38 μm^{-1} for the pyrrhotite mixture to 0.90 μm^{-1} for the siderite mixture. The S/V for the mixtures with high-concentration iron range from 0.58 μm^{-1} for the pyrrhotite mixture to 1.05 μm^{-1} for the siderite mixture

The iron-mineral surface-area-to-volume ratio S_M/V was determined by

$$\frac{S_M}{V} = \frac{S_M}{S}\frac{S}{V},$$ (9)

where S_M/S is the ratio of the iron-mineral surface area to the total surface area. S_M/S can be estimated from the specific mineral surface area S_{sM} by $S_M/S = yS_{sM}/S_s$, where y is the mass concentration

Table 4. The measured porosity ϕ and specific surface area S_S, and the calculated values for surface-area-to-volume ratio S/V, fractional mineral surface area S_M/S, and mineral-surface-area-to-volume ratio S_M/V. For the measured data, the values are the average of the measurements of three samples; the error is the standard deviation. For the calculated values, the error was calculated using error propagation. Entries with dashes indicate data were not available. The values for quartz sand are from Keating and Knight (2007).

Material	ϕ	S_s (m²/g)	S/V (μm^{-1})	S_M/S (m²/m²)	S_M/V (μm^{-1})
Quartz sand	0.48 ± 0.02	0.15 ± 0.02	0.48 ± 0.06	—	—
Low-concentration siderite mixture	0.49 ± 0.02	0.33 ± 0.04	0.90 ± 0.03	0.35 ± 0.11	0.31 ± 0.10
High-concentration siderite mixture	0.49 ± 0.02	0.38 ± 0.03	1.05 ± 0.03	0.61 ± 0.18	0.64 ± 0.19
Low-concentration pyrite mixture	0.48 ± 0.02	0.16 ± 0.07	0.50 ± 0.03	0.19 ± 0.08	0.09 ± 0.04
High-concentration pyrite mixture	0.48 ± 0.01	0.21 ± 0.05	0.59 ± 0.04	0.29 ± 0.11	0.17 ± 0.06
Low-concentration pyrrhotite mixture	0.50 ± 0.01	0.14 ± 0.03	0.38 ± 0.01	0.25 ± 0.17	0.10 ± 0.07
High-concentration pyrrhotite mixture	0.51 ± 0.01	0.22 ± 0.02	0.58 ± 0.01	0.32 ± 0.21	0.19 ± 0.13

of iron mineral. S_{sM} is determined from a linear fit to the equation

$$S_s = (1 - y)S_{sQ} + yS_{sM} = S_{sQ} + y(S_{sM} - S_{sQ}), \quad (10)$$

where S_{sQ} is the specific surface area of the quartz sand and S_s is the measured specific surface area for each iron-mineral type. For the linear fit, we use the measured value of S_{sQ} from Keating and Knight (2007).

The values of S_M/S and S_M/V are given in Table 4; both S_M/S and S_M/V are greater for the mixtures with higher iron concentrations. For the low-concentration mixtures, S_M/S ranges from 0.19 m^2/m^2 for the low-concentration pyrite samples to 0.35 m^2/m^2 for the low-concentration siderite samples, and S_M/V ranges from 0.09 μm^{-1} for the low-concentration pyrite samples to 0.31 μm^{-1} for the low-concentration siderite samples. For the high-concentration mixtures, S_M/S ranges from 0.29 m^2/m^2 for the high-concentration pyrite samples to 0.61 m^2/m^2 for the high-concentration siderite samples, and S_M/V ranges from 0.17 μm^{-1} for the high-concentration pyrite samples to 0.64 μm^{-1} for the high-concentration siderite samples. There are large errors associated with S_M/S and S_M/V that arise because of the linear fits to the S_s values and the low values for S_s of the samples.

Iron concentration

The measured Fe(II) and Fe(III) concentrations are shown in Table 5 for the siderite and pyrrhotite samples. All samples have a lower measured total iron concentration [i.e., Fe(II) + Fe(III) concentration] than the initial estimated concentration. The difference between the measured and estimated iron concentration likely results from the presence of impurities in the minerals, such as substitution for iron by other atoms within the crystal structure of the mineral. The difference between measured and estimated could also be caused by the dissolution of the minerals, the extent of which is variable, depending on the solubility of the mineral. Although siderite and pyrrhotite are soluble to some extent, siderite is more soluble in water than pyrrhotite (Lide, 2007). This explains the lower measured concentration of total iron in the siderite mixtures. For the pyrrhotite mixture, there was a large range in the iron concentration between samples (1.5% to >2% for the high-concentration pyrrhotite).

We previously have found that in samples with small grains and high magnetic susceptibility, the grains aggregate, which results in a nonuniform distribution of grains within subsamples and a large variation in the iron concentration between subsamples (Keating and Knight, 2008). Pyrrhotite has a high magnetic susceptibility, and the pyrrhotite grains were observed to aggregate during mixing; so we attribute the high variability in concentration between pyrrhotite subsamples to the nonuniform distribution of pyrrhotite grains within the subsamples.

The fact that the Fe(III) concentration in the siderite and pyrrhotite mixtures is nonzero indicates that some oxidation of Fe(II) to Fe(III) occurred. For the siderite mixtures, the Fe(III) content was 17% of the total iron content in the low-concentration samples and 13% of the total iron content in the high-concentration samples. Only a small concentration of Fe(III) was measured in the pyrrhotite sample; this is compatible with the XRD results, which show that a large portion of the pyrrhotite sample was in the form of troilite.

Total initial signal intensity

Before looking at the relaxation time distributions, we first considered the total initial signal intensity ΣI_{0i}. We are interested in looking at ΣI_{0i} to determine if the total water content is detected in the relaxation-time distribution curves. Although ΣI_{0i} is proportional to the total water content, the relative position on the y-axis is affected by the receiver gain, which changed between samples and the number of scans per sample. The sum of the total initial signal intensity from the repeated measurements for each sample, normalized by the receiver gain and the number of scans, was plotted versus the echo time for all of the iron mineral mixtures (Figure 2). Error bars, determined from the standard deviation of repeated measurements, are not shown because they are smaller than the size of the data points.

The variation in the total initial signal intensity between samples of a single concentration and iron mineral type results from differences in the water content; for example, the water content in the high-concentration pyrite samples varies from 9.73 to 10.22 ml. For the low-concentration siderite mixtures and for the high- and low-concentration pyrite mixtures, ΣI_{0i} does not show a trend with echo time or iron concentration. This indicates there was no signal loss with increase in echo time. However, for the high-concentration siderite mixtures and for the low- and high-concentration pyrrhotite mixtures, ΣI_{0i} decreases with echo time and with iron concentration. This observation indicates that a portion of the water in the high-concentration siderite samples and in the low- and high-concentration pyrrhotite samples relaxed before the initial NMR measurement, during the instrument dead time; so it was not detected and ΣI_{0i} does not provide information about the total water content.

Table 5. Estimated and measured iron content of siderite, pyrite, and pyrrhotite mixtures. The values shown are the average of the measurements of three samples; the error is the standard deviation. Entries with dashes indicate the data were not available.

Material	Estimated iron concentration (% g Fe/g sand)	Measured iron concentration (% g Fe/g sand)		
		Total Fe concentration	Fe(II) concentration	Fe(III) concentration
Low-concentration siderite mixture	1	0.6 ± 0.1	0.5 ± 0.1	0.10 ± 0.03
High-concentration siderite mixture	2	1.45 ± 0.01	1.26 ± 0.02	0.19 ± 0.01
Low-concentration pyrite mixture	1	—	—	—
High-concentration pyrite mixture	2	—	—	—
Low-concentration pyrrhotite mixture	1	0.7 ± 0.1	0.7 ± 0.1	0.03 ± 0.01
High-concentration pyrrhotite mixture	2	1.7 ± 0.5	1.7 ± 0.5	0.010 ± 0.005

Relaxation-time distributions

The NMR data set from each of the mixtures displays a multiexponential decay of signal intensity as described by equation 2. The raw decay curve was logarithmically subsampled to 5000 data points to improve the speed of the fitting procedure. The subsampled data were fit to a distribution of 200 exponentially spaced T_2 values ranging from 0.1 ms to 10 s using a nonnegative least-squares inversion routine with Tikhonov regularization (Whittall et al., 1991). The inversion parameters were selected such that each datum was misfit by approximately one standard deviation.

The T_2 distributions for one sample of each iron mineral and quartz mixture are shown in Figure 3 for $t_E = 300$ μs. The T_2 distributions are shown as the signal intensity normalized by the total signal intensity $I_{0i}/\Sigma I_{0i}$ for each sample versus the exponentially space T_{2i} values. Data from repeated measurements display similar distributions. Also shown in Figure 3d is the relaxation-time distribution for the pure quartz sand saturated with aerobic water as measured in Keating and Knight (2007). Saturating the quartz sample with anaerobic water would likely result in a small shift in the relaxation-time distribution toward longer relaxation times. The distributions for all iron-mineral and quartz mixtures are broader than the distribution for the quartz sand. In the next section, we discuss the general characteristics of the relaxation-time distributions. The exact shape of the relaxation-time distributions is a function of the smoothness constraints of the inversion algorithm, so we can only compare the distributions qualitatively.

The distributions for the siderite mixtures have two poorly resolved peaks, with one dominant peak and one smaller peak centered at shorter relaxation times (Figure 3a). The distribution for the low-concentration siderite mixture also shows an isolated peak at a relaxation time just below 1 s that we attribute to the presence of a small amount of standing water in the sample. If we compare the relaxation-time distributions of the low- and high-concentration siderite mixtures, the mixtures with high-concentration iron show a shift in the position of the dominant peak to shorter relaxation times and a broadening of the distribution.
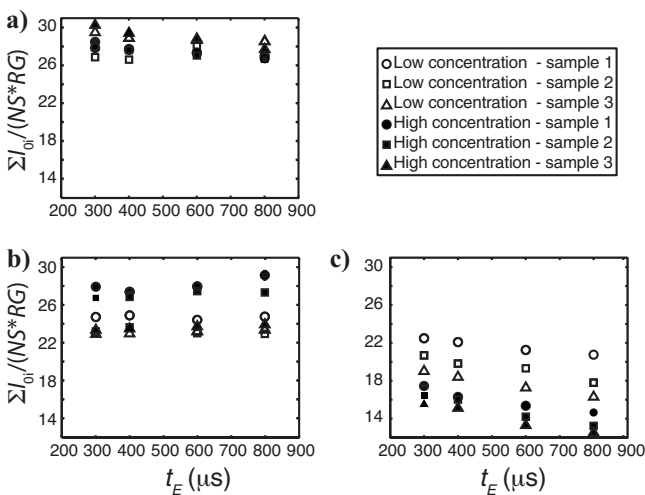
The distributions for the pyrite mixtures have two resolved peaks (Figure 3b). The mixtures with a high-concentration iron show a shift in the two resolved peaks toward shorter relaxation times. The distributions for the low-concentration mixtures have a small, poorly resolved peak at short relaxation times; this peak represents regions of faster relaxation.

The distributions for the pyrrhotite mixtures have no clearly resolved peaks and span more than two orders of magnitude of relaxation times (Figure 3c). Comparing the relaxation-time distributions for the high-concentration pyrrhotite mixtures with the relaxation-time distributions for the low-concentration mixtures, we see that the increase in iron concentration corresponds with a slight widening of the distribution but does not correspond with a change in the position of the distributions. We know we are not capturing some signal because of the observed trend in ΣI_{0i} with t_E; thus, there is water within the pyrrhotite sample that is relaxing with short relaxation times not represented in the relaxation-time distribution.

Mean log relaxation rates T_{2ML}^{-1}

The relaxation-time distribution was used to calculate T_{2ML}^{-1} for each sample. The T_{2ML}^{-1} values for each mixture are shown in Table 6 for an echo time of 300 μs. The values in Table 6 are the averages of values determined from measurements on the three samples of each mixture, and the errors are the standard deviation. Standing water observed at the top of some samples corresponded to an isolated peak at a relaxation time of approximately 1 s (e.g., Figure 3a); these isolated peaks were not included in the calculation of T_{2ML}^{-1}. We recognize that calculating T_{2ML}^{-1} for a wide distribution may not have as much meaning as calculating T_{2ML}^{-1} for a narrow distribution, but we feel that T_{2ML}^{-1} can identify and assess trends in the data.

Figure 2. Plots of the total recorded signal intensity ΣI_{0i} normalized by the receiver gain RG and the number of stacks NS versus the echo time t_E for each sample of the (a) siderite, (b) pyrite, and (c) pyrrhotite mixtures. Each plot shows the three samples measured for the low- and high-concentration mixtures. Error bars are not shown because they are smaller than the size of the data points.
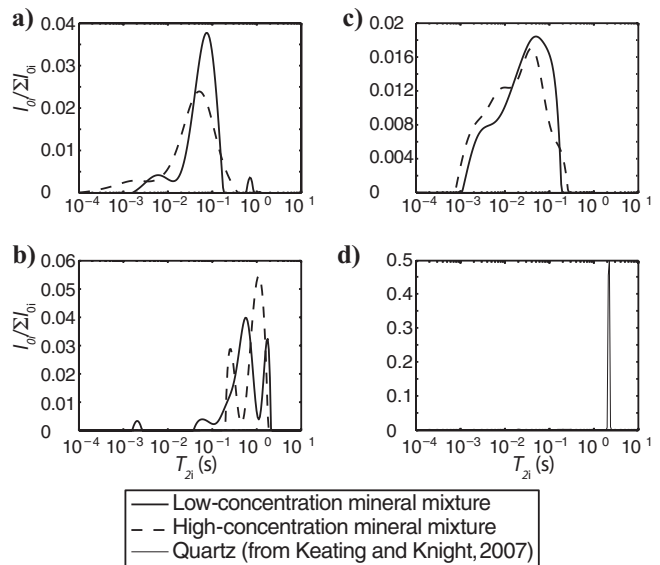

Figure 3. Relaxation time distributions for (a) siderite, (b) pyrite, and (c) pyrrhotite mixtures saturated with anaerobic water. The relaxation-time distributions shown are for the measurements made with an echo spacing of 300 μs; one measurement of the three samples measured is shown. (d) The relaxation-time distribution for the water-saturated quartz sand sample measured in Keating and Knight (2007), shown for reference. It was saturated with aerobic water.

Two observations were made for the calculated T_{2ML}^{-1} values: (1) for each iron mineral, T_{2ML}^{-1} is greater in the samples with the higher iron concentration and (2) T_{2ML}^{-1} varies between iron minerals. The dominant relaxation mechanism for each iron mineral can be determined by comparing the contribution of each relaxation rate to the mean log relaxation rate. The relaxation rates and the dominant relaxation mechanism are discussed in the following sections.

Bulk fluid relaxation rates T_{2B}^{-1}

The NMR relaxation rates for the bulk fluids, extracted from the samples, are given in Table 6. The values in Table 6 are the averages of values determined from measurements on the three samples of each mixture, and the errors are the standard deviation. To obtain these values of T_{2B}^{-1}, the NMR relaxation data for the extracted bulk fluids were fit using the same fitting procedure as for the measured iron-mineral mixtures. Each bulk fluid relaxation-time distribution consisted of a single, narrow peak. Theoretically, the bulk fluid relaxation-time distribution should consist of a single relaxation time; however, noise in the data and imperfect tuning of the excitation pulse result in a narrow distribution of relaxation-time values. The bulk fluid relaxation rate did not show any change with echo time.

The bulk fluid relaxation rate for the fluid extracted from each iron-mineral mixture is greater than the relaxation rate of deoxygenated, deionized water because of the introduction of paramagnetic species dissolved from the minerals. The paramagnetic species could be Fe(III) dissolved from the solid phase, Fe(III) oxidized from Fe(II) dissolved from the solid phase, or paramagnetic impurities dissolved from the mineral surface. The bulk fluid relaxation rates for the fluids extracted from the pyrite and pyrrhotite mixtures show a small range between 0.45 and 1.2 s^{-1} and do not correlate with mineralogic form or iron concentration. The fluids extracted from the siderite mixtures have much faster bulk fluid relaxation rates than the fluids extracted from the other mixtures, likely from the high solubility of siderite.

Diffusion relaxation rates T_{2D}^{-1}

The magnitude of the diffusion relaxation rate in the NMR response of a sample can be determined by measuring the dependence of T_{2ML}^{-1} on echo time. As can be seen from equations 3 and 4, a plot of T_{2ML}^{-1} versus t_E^2 yields a straight line with slope equal to $D(\gamma G)^2/12$. The intercept of this line is the sum of T_{2S}^{-1} and T_{2B}^{-1}.

Figure 4 shows this plot for the siderite, pyrite, and pyrrhotite mixtures. For each sample, the plotted data points are the average of the repeated measurements. Notably, although there is no increase with t_E^2 for the relaxation rates of the siderite and the pyrite mixtures (i.e., $G = 0$ within experimental accuracy), T_{2ML}^{-1} increases with t_E^2 for the pyrrhotite mixtures, indicating that protons in the pyrrhotite mixtures experience relaxation resulting from diffusion (i.e., $G \neq 0$).

The diffusion relaxation rates at $t_E = 300$ μs for the low- and high-concentration pyrrhotite mixtures are given in Table 6. The values of T_{2D}^{-1} given in Table 6 are the averages of the calculated values of T_{2D}^{-1} determined for the three samples of each iron-mineral mixture, and the errors are the standard deviation.

Surface relaxation rates T_{2S}^{-1}

The surface relaxation rates determined for each of the Fe(II)-mineral mixtures are shown in Table 6. The values of T_{2S}^{-1} given in Table 6 are the averages of the calculated values of T_{2S}^{-1} determined for the three samples of each iron-mineral mixture, and the errors are the standard deviation. There is a large range in the T_{2S}^{-1} values, from 0.56 s^{-1} for the low-concentration pyrite mixture to 77 s^{-1} for the high-concentration pyrrhotite samples. The T_{2S}^{-1} values are greater for each of the Fe(II) mineral mixtures than is the T_{2S}^{-1} value for the quartz sand. For each iron mineral, the T_{2S}^{-1} values are greater for the samples with higher iron concentration.

Dominant relaxation mechanism

To determine the dominant relaxation mechanism for each mixture, we compared the transverse relaxation rates T_{2B}^{-1}, T_{2D}^{-1}, and

Table 6. Relaxation rates and surface relaxivity for the iron-mineral mixtures. For the relaxation rates, the values are the average of the values from three samples; the error is the standard deviation. For surface relaxivity, the error was calculated using error propagation. Entries with dashes indicate data were not available. The values for T_{2ML}^{-1} and T_{2D}^{-1} are given for an echo time of 300 μs. Values for quartz sand are from Keating and Knight (2007).

Material	T_{2ML}^{-1} (s^{-1})	T_{2B}^{-1} (s^{-1})	T_{2S}^{-1} (s^{-1})	T_{2D}^{-1} (s^{-1})	ρ_2 (μm s^{-1})	$\rho_2 a/D$	ρ_{2M} (μm s^{-1})	$\rho_{2M} a/D$
Anaerobic water	—	0.26 ± 0.01	—	—	—	—	—	—
Quartz sand	0.49 ± 0.02	0.328 ± 0.005	0.16 ± 0.02	0	0.31 ± 0.04	—	—	—
Low-concentration siderite mixture	22.5 ± 0.5	6 ± 2	17 ± 1	0	$\geq 19 \pm 2^a$	1.1	$\geq 54 \pm 10^a$	2.8
High-concentration siderite mixture	33 ± 1	5.6 ± 0.7	27.4 ± 0.8	0	$\geq 26.0 \pm 0.1^a$	1.5	$\geq 43 \pm 2^a$	2.2
Low-concentration pyrite mixture	1.5 ± 0.6	1.2 ± 0.7	0.56 ± 0.07	0	1.2 ± 0.1	0.07	6 ± 0.6	0.38
High-concentration pyrite mixture	1.7 ± 0.5	0.45 ± 0.07	1.2 ± 0.2	0	1.8 ± 0.4	0.11	7 ± 1	0.34
Low-concentration pyrrhotite mixture	48 ± 3	0.48 ± 0.1	45 ± 4	5 ± 2	$\geq 120 \pm 10^a$	7.03	$\geq 474 \pm 60^a$	35
High-concentration pyrrhotite mixture	82 ± 17	0.66 ± 0.06	77 ± 17	6.7 ± 0.7	$\geq 140 \pm 30^a$	8.20	$\geq 417 \pm 90^a$	31

[a]Relaxation of water in these samples did not occur in the fast diffusion regime.

$T_{2S}{}^{-1}$. The percent contributions from each relaxation rate are plotted as a stacked bar graph in Figure 5. From Figure 5, we see that, for the low- and high-concentration siderite mixtures, $T_{2B}{}^{-1}$ is not the dominant relaxation mechanism, but it does account for a large portion of the total relaxation rate. $T_{2B}{}^{-1}$ accounts for 20–32% of $T_{2ML}{}^{-1}$ in the three siderite samples with low-concentration iron and 15–19% of $T_{2ML}{}^{-1}$ in the three siderite samples with high-concentration iron. For the low-concentration pyrite samples, $T_{2B}{}^{-1}$ is the dominant relaxation mechanism and accounts for 67–78% of $T_{2ML}{}^{-1}$ in the three measured samples. For the high-concentration pyrite samples, bulk fluid relaxation is not the dominant relaxation mechanism but does account for 23–34% of $T_{2ML}{}^{-1}$ in the three measured samples. For the pyrrhotite mixtures, bulk fluid relaxation is not the dominant relaxation mechanism; for each of the pyrrhotite samples, $T_{2B}{}^{-1}$ is about 1% of $T_{2ML}{}^{-1}$. Comparing $T_{2D}{}^{-1}$ to $T_{2ML}{}^{-1}$ for the pyrrhotite minerals at $t_E = 300$ μs, we find that the diffusion relaxation accounts for less than 10% of the total relaxation rate and is not the dominant relaxation mechanism.

If instead we compare $T_{2S}{}^{-1}$ to $T_{2ML}{}^{-1}$, we find that surface relaxation is the dominant relaxation mechanism for the siderite mixtures, the high-concentration pyrite mixtures, and the pyrrhotite mixtures. For the three measured siderite samples with low-concentration iron, $T_{2S}{}^{-1}$ accounts for 65–79% of $T_{2ML}{}^{-1}$; for the three measured siderite samples with a high concentration, $T_{2S}{}^{-1}$ accounts for 81–85% of $T_{2ML}{}^{-1}$. For the high-concentration pyrite mixtures, the surface relaxation mechanism dominates with $T_{2S}{}^{-1}$ accounting for more than 65% of $T_{2ML}{}^{-1}$ for the three measured samples. For all measured pyrrhotite samples (low and the high concentration), $T_{2S}{}^{-1}$ accounts for more than 90% of $T_{2ML}{}^{-1}$. For the low-concentration pyrite mixtures, the bulk fluid relaxation mechanism plays a much more significant role than the surface relaxation, with $T_{2S}{}^{-1}$ accounting for less than 35% of $T_{2ML}{}^{-1}$ for the three measured samples.

Surface relaxivity and diffusion regime

We begin by assuming that the relaxation of all of the samples can be described as falling within the fast diffusion regime, and we calculate the surface relaxivity using equation 5. The surface relaxivity values for the mineral mixtures are given in Table 6; the errors for ρ_2 were calculated from error propagation. We then test the assumption of fast diffusion by calculating $\rho_2 a/D$; a value less than one would indicate that the assumption is valid. Although we have calculated ρ_2 for each sample and D is known, obtaining a is challenging. The parameter a, defined as the pore radius, provides a measure of the mean distance that a proton would need to travel to reach a paramagnetic site. A common method of calculating a is to assume that $a = (S/V)^{-1}$, where S/V is for the entire sample (e.g., Dunn et al., 2002). Using this method to calculate a gives values between 0.9 and 2.7 μm for all mixtures; these values of a imply that the pore radii are less than 2% of the size of the quartz grains and are clearly too small.

If we consider the schematic of the pore space given in Figure 1, where the iron-mineral grains are much smaller than the quartz grains and there is more than one iron-mineral grain in each pore space, a more realistic method to calculate a would be to assume that the quartz grains provide a framework for the solid medium and to calculate the pore radius of the quartz framework. If we use $a = (S_Q/V)^{-1}$, where S_Q/V represents the surface-area-to-volume ratio for a packed quartz grain sample (the value of S_Q/V is determined by Keating and Knight [2008]), we obtain values for $\rho_2 a/D$ that are much less than one for all the of mixtures. However, the value of a calculated from this method is 2.083 μm, which is 1% of the size of the quartz grain radius; this again is too small and reflects the roughness of the solid surface.

We have instead chosen to estimate a in a way that provides an upper limit on the pore radius. We estimate a using the radius of the maximum inscribable sphere in a simple cubic packing of quartz grains. Guillot (1982) shows that the radius of the maximum inscribable sphere inside a simple cubic packing is $a = 0.732r$, where r is the radius of a grain ($r = 200$ μm). The value of a estimated in this manner is 146.4 μm.

The values for $\rho_2 a/D$, given in Table 6, show that the fast-diffusion-regime assumption is correct only for the pyrite mixtures but
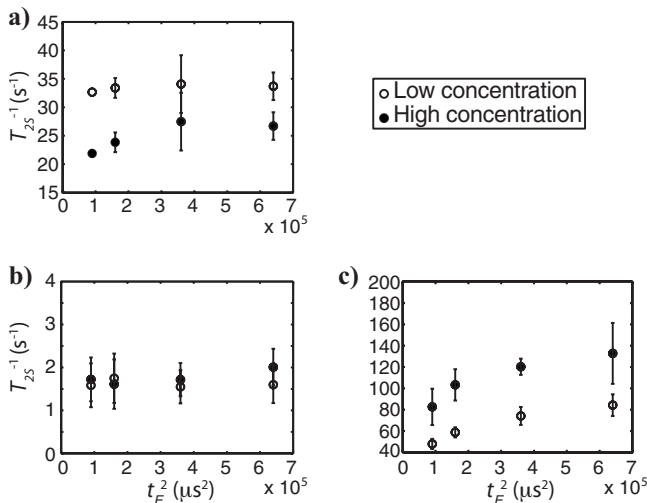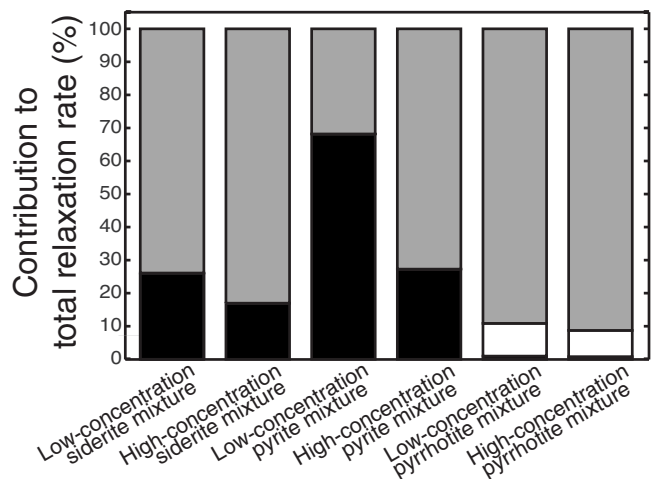
Figure 4. Plots of relaxation rate versus echo time squared for (a) siderite, (b) pyrite, and (c) pyrrhotite mixtures. Each plot shows the average relaxation rate for the three samples measured for the low- and high-concentration mixtures. The data points are the mean of calculated $T_{2ML}{}^{-1}$ values from the three samples, and the error bars are calculated from the standard deviation. Error bars not shown are smaller than the size of the data point.

Figure 5. Stacked bar graph showing the relative contributions of $T_{2BL}{}^{-1}$ (black bar), $T_{2DL}{}^{-1}$ (white bar), and $T_{2SL}{}^{-1}$ (gray bar) as a percent of the total relaxation rate $T_{2ML}{}^{-1}$ for each iron-mineral mixture.

does not hold for the siderite and pyrrhotite mixtures. The relaxation of the siderite and pyrrhotite mixtures appears to occur in the intermediate diffusion regime, which has two implications for analysis of the relaxation measurements. First, the relaxation-time distribution for the siderite and pyrrhotite mixtures does not represent a true pore-environment distribution. Second, the surface relaxivity values calculated for the siderite and pyrrhotite mixtures are not true surface relaxivity values but are lower bounds on the surface relaxivity values. In other words, for siderite we find $\rho_2 \geq 19 \ \mu\text{m/s}$ and $\rho_2 \geq 26 \ \mu\text{m/s}$, and for pyrrhotite we find $\rho_2 \geq 120 \ \mu\text{m/s}$ and $\rho_2 \geq 140 \ \mu\text{m/s}$.

The ρ_2 values determined for the mineral mixtures show that for the pyrite mixtures, ρ_2 is larger for the high-concentration pyrite mixture. Similarly, the lower bound on the siderite and pyrrhotite mixtures is larger for the high-concentration mixtures.

Our earlier study (Keating and Knight, 2007) determines the ρ_2 values for 1% Fe(III)-bearing mineral-coated quartz sands and 0.65% mixed-valence iron mineral-coated quartz sands (Tables 2 and 3). Because the spin number for Fe(II) is less than the spin number for Fe(III), we would expect the ρ_2 values measured in the current study to be less than the ρ_2 values measured in our previous study. The diffusion regimes for the samples we measured (Keating and Knight, 2007) are calculated using $a = V/S$; recalculating the diffusion regimes using the method outlined in our current paper shows that all samples are in the fast diffusion regimes except for the 1% hematite mixtures and the 0.65% magnetite mixtures.

Comparing the ρ_2 values from our two studies, we find that the ρ_2 value for the low-concentration pyrite mixture is less than the ρ_2 values for the Fe(III) and mixed-valence iron-coated sands previously measured. The ρ_2 value for the high-concentration pyrite mixture is in the range of ρ_2 for the Fe(III) and mixed-valence iron-coated sands. For the low-concentration siderite and pyrite mixtures, we know the lower bounds on ρ_2 are 19 and 120 μm/s, respectively; so ρ_2 for these minerals falls within or is greater than ρ_2 for the iron-coated sands previously measured (Tables 2 and 3). The variation in the surface relaxivity between mineralogic forms most likely reflects differences in the spin number associated with impurities in the mineral (e.g., manganese, magnesium, cobalt, nickel), the density and distribution of paramagnetic species on the surface of the pores, and the distance between relaxing protons and the paramagnetic species (Godefroy et al., 2001). Identifying and quantifying the specific property of an iron mineral that determines the magnitude of the surface relaxivity is a topic for further research.

We next determine ρ_{2M}. We again begin by assuming that the relaxation of all of the samples falls within the fast diffusion regime, but we now calculate ρ_{2M} using equation 6. The values for ρ_{2M} are given in Table 6; the errors for ρ_{2M} were calculated from error propagation. We then test the assumption of fast diffusion by calculating $\rho_{2M}a/D$. The values for $\rho_{2M}a/D$, given in Table 6, again show that the fast-diffusion-regime assumption is only correct for the pyrite mixtures but does not hold for the siderite and pyrrhotite mixtures. The relaxation of the siderite mixtures appears to occur in the intermediate diffusion regime, and the relaxation for the pyrrhotite mixtures appears to occur in the slow diffusion regime. The ρ_{2M} values calculated for the siderite and pyrrhotite mixtures are not true ρ_{2M} values but are lower bounds on the ρ_{2M} values, i.e., for siderite, we find $\rho_{2M} \geq 54 \ \mu\text{m/s}$ and $\rho_{2M} \geq 43 \ \mu\text{m/s}$; for pyrrhotite, we find $\rho_{2M} \geq 474 \ \mu\text{m/s}$ and $\rho_{2M} \geq 417 \ \mu\text{m/s}$. The large error values associated with the values of ρ_{2M} were calculated from error propagation and result from the large errors associated with S_M/V.

Comparing the values determined for ρ_2 to the values determined for ρ_{2M} we make the following observations: (1) for all samples, $\rho_2 < \rho_{2M}$, as expected; (2) for the pyrite samples, relaxation occurs in the fast diffusion regime using ρ_2 and ρ_{2M} to determine the diffusion regime; (3) for the siderite samples, relaxation occurs in the intermediate diffusion regime using ρ_2 and ρ_{2M} to determine the diffusion regime; (4) for the pyrrhotite samples, relaxation appears to occur in the intermediate diffusion regime if ρ_2 is used to determine the diffusion regime, and relaxation appears to occur in the slow diffusion regime if ρ_{2M} is used to determine the diffusion regime. Finally, to determine if relaxation occurs in the intermediate diffusion regime, accurate values of $\rho_{2M}a/D$ and ρ_2a/D (within one order of magnitude) are required. Given the large uncertainty associated with the values for a and ρ_{2M} used to calculate $\rho_{2M}a/D$ and $\rho_{2M}a/D$, there is also large uncertainty associated with assigning the intermediate diffusion regime as the regime in which relaxation occurs.

SUMMARY AND CONCLUSIONS

The following results were obtained from this study: (1) When considered for a single iron mineral, $T_{2ML}{}^{-1}$ and $T_{2S}{}^{-1}$ are greater for mineral mixtures with higher Fe(II) concentration. (2) Surface relaxation was the dominant relaxation mechanism for both concentrations of the pyrrhotite and siderite mixtures and the high-concentration pyrite mixtures. However, bulk fluid relaxation played a significant role in all siderite and pyrite samples and was the dominant relaxation mechanism for the low-concentration pyrite mixtures. (3) $T_{2D}{}^{-1}$ is zero for the siderite and pyrite mixtures but nonzero for the pyrrhotite mixtures. (4) The surface relaxivity calculations revealed that relaxation occurs in the fast diffusion regime for the pyrite mixture and relaxation occurs in the intermediate diffusion regime for the siderite mixtures. For the pyrrhotite mixtures, using the ρ_2 values showed that relaxation occurs in the intermediate diffusion regime, and using the ρ_{2M} values showed that relaxation occurs in the slow diffusion regime. Large uncertainty is associated with assigning the intermediate regime as the regime in which relaxation occurs. (5) The values of ρ_2 and ρ_{2M} exhibited a large range between iron minerals. For the pyrrhotite mixtures, where diffusion relaxation contributes to total relaxation, the relaxation rates measured at other magnetic field strengths could be different than the rates measured in this study.

We conclude that NMR relaxation rates, although affected by the concentration of Fe(II) and/or Fe(III), will also vary as a result of changes in the mineralogic form of the iron. This observation supports our earlier published conclusion that the mineralogic form of the iron, and not just the iron concentration, is an important factor in determining relaxation rates and surface relaxivity. Although the results of our study provide significant insight into the NMR properties of Fe(II)-bearing minerals, further research is required to develop a fundamental understanding of how and why mineralogic form influences NMR relaxation rates, to understand the effect of other common paramagnetic species (e.g., manganese) on the NMR relaxation rates, to determine experimentally the correct a value that should be used when calculating the relaxation regime, and to understand the effect of magnetic field strength on the diffusion relaxation rate.

ACKNOWLEDGMENTS

REFERENCES

Abragam, A., 1961, The principles of nuclear magnetism: Oxford University Press.

Anand, A., and G. J. Hirasaki, 2008, Paramagnetic relaxation in sandstones: Distinguishing T_1 and T_2 dependence on surface relaxation, internal gradients and dependence on echo spacing: Journal of Magnetic Resonance, **190**, 68–85.

Arns, C. H., 2004, A comparison of pore size distributions derived by NMR and X-ray-CT techniques: Physica A, **339**, 159–165.

Babes, L., B. Denizot, G. Tanguy, J. J. Le Jeune, and P. Jallet, 1999, Synthesis of iron oxide nanoparticles used as MRI contrast agents: A parametric study: Journal of Colloid and Interface Science, **212**, 474–482.

Bloembergen, N., E. M. Purcell, and R. V. Pound, 1948, Relaxation effects in nuclear magnetic resonance absorption: Physical Review, **73**, 679–715.

Brown, R. J. S., and B. W. Gamson, 1960, Nuclear magnetism logging: Transactions of the American Institute of Mining, Metallurgy and Petroleum Engineers, **219**, 199–207.

Brownstein, K. R., and C. E. Tarr, 1979, Importance of classical diffusion in NMR studies of water in biological cells: Physical Review A, **19**, 2446–2453.

Bryar, T. R., C. J. Daughney, and R. J. Knight, 2000, Paramagnetic effects of iron(III) species on nuclear magnetic relaxation of fluid protons in porous media: Journal of Magnetic Resonance, **142**, 74–85.

Bryar, T. R., and R. J. Knight, 2002, Sensitivity of nuclear magnetic resonance relaxation measurements to changing soil redox conditions: Geophysical Research Letters, **29**, 50-1–50-4.

———, 2003, Laboratory studies of the effect of sorbed oil on proton nuclear magnetic resonance: Geophysics, **68**, 942–948.

Carr, H. Y., and E. M. Purcell, 1954, Effects of diffusion on free precession in nuclear magnetic resonance experiments: Physical Review, **94**, 630–638.

Clayton, N., 2006, Oilfield developed geophysical logging in cased and uncased wells for high-resolution characterization of an alluvium ASR system in the Central Valley, California: Presented at the Hydrogeophysics Workshop, SEG.

Coey, J. M. D., 1988, Magnetic properties of iron in soil iron oxides and clay minerals, *in* J. W. Stucki, B. A. Goodman, and U. Schwertmann, eds., Iron in soils and clay minerals: D. Reidel Publishing Co., 397–466.

Cornell, R. M., and U. Schwertmann, 2003, The iron oxides: Structure, properties, reactions, occurrences and uses, 2nd ed.: Wiley-VCH.

Dunn, K.-J., D. J. Bergman, and G. A. Latorraca, 2002, Nuclear magnetic resonance petrophysical and logging applications: Pergamon Press, Inc.

Foley, I., S. A. Farooqui, and R. L. Kleinberg, 1996, Effect of paramagnetic ions on NMR relaxation of fluids at solid surfaces: Journal of Magnetic Resonance, **123**, 95–104.

Gillis, P., and S. H. Koenig, 1987, Transverse relaxation of solvent protons induced by magnetized spheres: Application to ferritin, erythrocytes and magnetite: Magnetic Resonance in Medicine, **5**, 323–345.

Godefroy, S., J.-P. Korb, M. Fleury, and R. G. Bryant, 2001, Surface nuclear magnetic relaxation and dynamics of water and oil in macroporous media: Physical E, **64**, 21605-21601–21605-21613.

Gossuin, Y., R. N. Muller, and P. Gillis, 2004, Relaxation induced by ferritin: A better understanding for an improved MRI iron quantification: NMR in Biomedicine, **17**, 427–432.

Gossuin, Y., A. Roch, R. N. Muller, P. Gillis, and F. Lo Bue, 2002, Anomalous nuclear magnetic relaxation of aqueous solutions of ferritin: An unprecedented first-order mechanism: Magnetic Resonance in Medicine, **48**, 959–964.

Guillot, D., 1982, Propriètés physiques et texturales d'un modèle artificiel de matèriau à porosité intergranulaire: Thesis, Mines de Paris.

Hunt, C. P., B. M. Moskowitz, and S. K. Banerjee, 1995, Magnetic properties of rocks and minerals, *in* T. J. Ahrens, ed., Rock physics and phase relations: A handbook of physical constants: American Geophysical Union, 189–204.

Hurlimann, M. D., L. Venkataramanan, C. Flaum, P. Speier, C. Karmonik, R. Freedman, and N. Heaton, 2002, Diffusion-editing: New NMR measurement of saturation and pore geometry: 43rd Annual Logging Symposium, Society of Professional Well Log Analysts, Paper FFF.

Jaeger, F., E. Grohmann, and G. E. Schaumann, 2006, ^{1}H NMR relaxometry in natural humous soil samples: Insights in microbial effects on relaxation time distributions: Plant Soil, **280**, 209–222.

Keating, K., and R. J. Knight, 2007, A laboratory study to determine the effect of iron oxides on proton NMR measurements: Geophysics, **72**, no. 1, E27–E32.

———, 2008, A laboratory study of the effects of magnetite on NMR relaxation rates: Journal of Applied Geophysics, **66**, 188–196.

Keating, K., R. J. Knight, and K. Tufano, 2008, Nuclear magnetic resonance relaxation measurements as a means of monitoring iron mineralization processes: Geophysical Research Letters, **35**, L19405.

Klein, C., 2002, The manual of mineral science, 22nd ed.: John Wiley & Sons, Inc.

Kleinberg, R. L., 2001, Data interpretation and reservoir analysis: NMR measurements of physical properties: Concepts in Magnetic Resonance, **13**, 404–406.

Kleinberg, R. L., and M. A. Horsfield, 1990, Transverse relaxation processes in porous sedimentary rock: Journal of Magnetic Resonance, **88**, 9–19.

Kleinberg, R. L., W. E. Kenyon, and P. P. Mitra, 1994, Mechanism of NMR relaxation of fluids in rock: Journal of Magnetic Resonance Series A, **108**, 206–214.

Kleinberg, R. L., A. Sezinger, D. D. Griffin, and M. Fukuhara, 1992, Novel NMR apparatus for investigating an external sample: Journal of Magnetic Resonance, **97**, 466–485.

Legchenko, A., J.-M. Baltassat, A. Bobachev, C. Martin, H. Robain, and J.-M. Vouillamoz, 2004, Magnetic resonance sounding applied to aquifer characterization: Ground Water, **42**, 363–373.

Lide, D., 2007, CRC handbook of chemistry and physics, 88th ed.: CRC Press.

Meiboom, S., and D. Gill, 1958, Modified spin-echo method for measuring nuclear relaxation times: Review of Scientific Instruments, **29**, 688–691.

Pratt, A. R., I. J. Muir, and H. W. Nesbitt, 1994, X-ray photoelectron and Auger electron spectroscopic studies of pyrrhotite and mechanism of air oxidation: Geochimica et Cosmochimica Acta, **58**, 827–841.

Schirov, M., A. Legchenko, and G. Creer, 1991, New direct non-invasive ground water detection technology for Australia: Exploration Geophysics, **22**, 333–338.

Senturia, S. D., and J. D. Robinson, 1970, Nuclear spin-lattice relaxation of liquids confined in porous solids: Society of Petroleum Engineers Journal, **10**, 237–244.

Song, Y.-Q., 2003, Using internal magnetic fields to obtain pore size distributions of porous media: Concepts in Magnetic Resonance, **18A**, 97–110.

Stingaciu, L. R., A. Pohlmeier, P. Blümler, L. Weihermüller, D. Van Dusschoten, S. Stapf, and H. Vereecken, 2009, Characterization of unsaturated porous media by high-field and low-field NMR relaxometry: Water Resources Research, **45**, W08412.

Stookey, L. L., 1970, Ferrozine — A new spectrophotometric reagent for iron: Analytical Chemistry, **42**, 779–781.

Timur, A., 1969, Pulsed nuclear magnetic resonance studies of porosity, movable fluid, and permeability of sandstone: Journal of Petroleum Technology, **21**, 755–786.

Vogeley, J. R., and C. O. Moses, 1992, ^{1}H NMR relaxation and rock permeability: Geochimica et Cosmochimica Acta, **56**, 2947–2953.

Whittall, K. P., M. J. Bronskill, and R. M. Henkelman, 1991, Investigation of analysis techniques for complicated NMR relaxation data: Journal of Magnetic Resonance, **95**, 221–234.

Yilmaz, A., M. Bucciolini, G. Longo, F. Franciolini, L. Ciraolo, and R. Renzi, 1990, Determination of dependence of spin-lattice relaxation rate in serum upon concentration of added iron by magnetic resonance imaging: Clinical Physics and Physiological Measurement, **11**, 343–349.

Zhang, G. Q., G. J. Hirasaki, and W. V. House, 2003, Internal field gradients in porous media: Petrophysics, **44**, 422–434.